Reports on Progress in **Physics**

PURPOSE-LED PUBLISHING™

PAPER • OPEN ACCESS

How semiconducting are ferroelectrics: the fundamental, optical and transport gaps of $Na_{0.5}Bi_{0.5}TiO_3$–$BaTiO_3$ and $NaNbO_3$

To cite this article: Pengcheng Hu *et al* 2026 *Rep. Prog. Phys.* **89** 028004

View the article online for updates and enhancements.

You may also like

- Autler–Townes splitting in Rydberg atoms: transition dipole matrix element extraction and field efficiency analysis
Brian C Holloway, Gavin M Chase, Lee E Harrell et al.

- ICRH modelling of DTT in full power and reduced-field plasma scenarios using full wave codes
A Cardinali, C Castaldo, F Napoli et al.

- Probing flying-focus wakefields
Aaron Liberman, Anton Golovanov, Sheroy Tata et al.

This content was downloaded from IP address 86.58.13.110 on 07/04/2026 at 12:32

IOP Publishing Rep. Prog. Phys. 89 (2026) 028004 https://doi.org/10.1088/1361-6633/ae464c

Reports on Progress in Physics

OPEN ACCESS

RECEIVED
7 December 2025

REVISED
27 January 2026

ACCEPTED FOR PUBLICATION
16 February 2026

PUBLISHED
2 March 2026

Original content from this work may be used under the terms of the Creative Commons Attribution 4.0 licence.

Any further distribution of this work must maintain attribution to the author(s) and the title of the work, journal citation and DOI.

PAPER

How semiconducting are ferroelectrics: the fundamental, optical and transport gaps of $Na_{0.5}Bi_{0.5}TiO_3$–$BaTiO_3$ and $NaNbO_3$

Pengcheng Hu[1], Nicole Bein[1], Chinmay Chandan Parhi[2], Tadej Rojac[3], Barbara Malič[3], Mohammad Amirabbasi[4], Anton Volodin[4], Karsten Albe[4], Jurij Koruza[2] and Andreas Klein[1,*]

[1] Institute of Materials Science, Electronic Structure of Materials, Technical University of Darmstadt, Otto-Berndt-Str 3, Darmstadt 64287, Germany
[2] Institute for Chemistry and Technology of Materials, Graz University of Technology, Stremayrgasse 9, Graz 8010, Austria
[3] Electronic Ceramics Department, Jožef Stefan Institute, Jamova cesta 39, Ljubljana 1000, Slovenia
[4] Institute of Materials Science, Materials Modelling, Technical University of Darmstadt, Otto-Berndt-Str. 3, Darmstadt 64287, Germany
[*] Author to whom any correspondence should be addressed.

E-mail: aklein@esm.tu-darmstadt.de

Keywords: ferroelectrics, band gap, photoelectron spectroscopy, polarons, excitons

Corresponding editor: Dr Lorna Brigham

Abstract

The energy gap is a fundamental property of materials, directly related to their optical and electronic properties. The energy gap of ferroelectric compounds and its adjustment by compositional variation has particularly attracted attention in recent years due to potential application in energy conversion and/or catalytic devices. It is demonstrated that it is necessary to distinguish between the fundamental gap, E_g^0, the optical gap, E_g^{opt}, and the transport gap, E_g^{tr}, of ferroelectrics, which can differ significantly. The situation is comparable to those in organic semiconductors and emerges from the presence of localized charges. The fundamental gap is a ground state property, i.e. the energy difference between the maximum of the fully occupied valence band and the minimum of the completely empty conduction band. In contrast, the optical and transport gaps are excited state properties involving localized (polaronic) electrons and/or holes at energies considerably different from the band edges. This work illustrates how the different energy gaps of ferroelectrics can be determined by combining optical measurements, x-ray photoelectron spectroscopy and temperature and oxygen partial pressure dependent electrical conductivity measurements. We determine fundamental gaps of ≈ 4.5 eV for both materials, optical gaps of 3.25–3.45 eV/3.5 eV and electrical gaps of ≈ 1.4 eV/3.3 eV for $Na_{0.5}Bi_{0.5}TiO_3$–$BaTiO_3$/$NaNbO_3$, respectively.

1. Introduction

1.1. Semiconducting ferroelectrics

The opto-electronic properties of materials are intimately connected to their electronic structure [1, 2]. The energy gap, which separates occupied valence bands from unoccupied conduction bands, is crucial for opto-electronic applications such as photodetectors, solar cells, light-emitting diodes, semiconductor lasers and photocatalysts. All these applications are enabled by semiconducting materials, in which electrical and optical properties are governed by the electronic structure of the valence and conduction band and their occupation by electronic charge carriers. In the ground state, occupied states at the top of the valence band are separated from empty states at the minimum of the conduction band by the fundamental energy gap. In semiconductors, the occupation of the valence and conduction band by holes and electrons is conventionally described by the occupation of electronic states, which do not change their energy upon occupation of the state. In this case, the optical and transport gaps, which are related to optical and thermal transitions of electronic carriers, respectively, are identical to the fundamental gap as illustrated in figure 1.

© 2026 The Author(s). Published by IOP Publishing Ltd

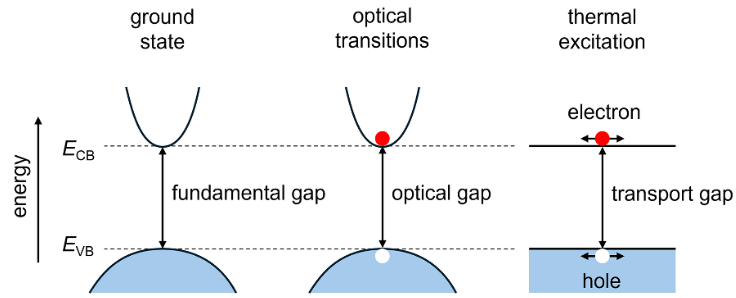

Figure 1. The energy gaps in classical semiconductors. The fundamental gap separates the occupied states in the valence band from the unoccupied states in the conduction band. The energies of the states do not change when the states are occupied by electrons or holes. The fundamental gap is therefore also relevant for optical transitions and the thermal generation of mobile charge carriers.

In ferroelectric materials, which exhibit spontaneous polarization switchable in symmetry-determined crystallographic directions, (free) electrons and holes in the conduction and valence bands have been invoked to discuss conductive domain walls or photocatalytic effects [3–5] (see figure 2(a)). In both cases, (free) electrons and holes are employed to compensate for the bound polarization charges of $\approx 40\,\mu\mathrm{C\,cm^{-2}}$, which terminate ferroelectric domains. However, Fridkin already stated that the concentration of free electrons and holes in ferroelectrics is typically negligible as the electronic charge carriers are trapped [6]. In more ionically bonded solids, such as ferroelectric oxides, ionic defects and trapped electrons and holes need to be taken into account as well [7]; these are also referred to as polarons. Trapped electronic charge carriers are also discussed for charge transport in ferroelectrics [8–12], but their role in the energy band diagram and their connection to the energy gap are hardly considered. Figure 2 illustrates some anticipated consequences of trapped charge carriers on the polarization screening by mobile electronic carriers. There are two major differences between free and trapped charge carriers: (i) the concentration of free electrons as determined by the occupation of the electronic states near the edges is connected to the effective density of states in the bands [1]:

$$N_{\mathrm{V,C}} = 2\left(\frac{2\pi\, m^{*}_{\mathrm{h,e}} k_{\mathrm{B}} T}{h^{2}}\right)^{3/2}, \tag{1}$$

where k_{B}, T, and h are Boltzmann's constant, temperature, and Planck's constant, and $m_{\mathrm{e,h}}$ correspond to the effective masses of holes and electrons, respectively. For typical values of the effective masses of 1–5, the effective density of states is $\approx 10^{19}\,\mathrm{cm^{-3}}$. This value is orders of magnitude lower than the density of polaron sites, which is equal to the atom density of the trapping species ($\approx 10^{22}\,\mathrm{cm^{-3}}$). Due to the low density of states of free electrons/holes, the width of the region required to provide the charges for screening polarization ($\approx 40\,\mu\mathrm{C\,cm^{-2}}$) is several 100 nm [3, 4]. In contrast, a unit cell thick layer is sufficient in the case of trapped charges; ii) The variation of the Fermi level ranges from the valence band maximum (VBM) to the conduction band minimum (CBM) in the case of free charges. For trapped charges, the Fermi level can only vary between the electron's and the hole's polaron levels, which will limit, e.g. the photovoltages developing upon illumination. The differences in polarization screening by free/trapped charges are illustrated by energy band diagrams in figure 2.

The effect of trapped electronic charges on transport properties is straightforward, but their role on optical transitions is less clear and likely also depends on the material. The underlying effects are particular crucial for optoelectronic and photocatalytic applications of ferroelectrics [14–20]. A major issue of ferroelectrics is their low sensitivity to visible light, as their 'energy gaps', determined by optical techniques, are typically > 3 eV. Tuning the energy gap hence became an important issue [19, 21]. Therefore, it is inevitable to understand the nature of the band gap, particularly what is measured by optical techniques, and how this gap relates to the energy levels involved in electrical transport and the fundamental gap from standard density functional theory calculations.

1.2. The nature of the energy gap

Traditionally, the energy gap is measured by optical techniques such as transmission, reflectance and/or ellipsometry [22]. For non-transparent polycrystalline ferroelectrics, diffuse reflectance (DR) with an application of the Kubelka–Munk evaluation and Tauc plots is often the method of choice [23, 24]. This technique employs an optical transition and inducing the formation of an electron–hole pair. The resulting excited state has to be distinguished from the ground state, which corresponds to a fully occupied

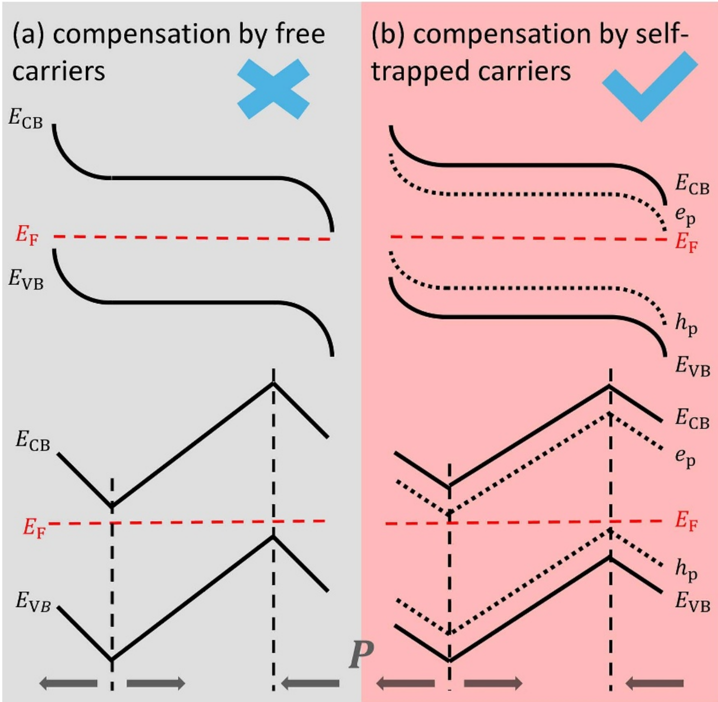

Figure 2. Energy band diagrams for a ferroelectric material with polarization (P) and charged domain walls, as proposed in [5, 13], where the polarization is compensated by free electrons and holes and the Fermi level varies through the complete energy gap (a); (b) hypothetical energy band diagram with upper and lower Fermi energy limits determined by self-trapped electrons and holes, where the polarization is compensated by trapped charges and the Fermi level varies only between the electron's and the hole's polaron levels e_p and h_p.

valence band and a completely empty conduction band. The term *fundamental energy gap* is used here for the energy difference between VBM, E_{VB}, and CBM, E_{CB}, in the ground state. The fundamental gap related to the ground state of a material is denoted in this manuscript as E_g^0.

An important modification of the electronic states from their ground state is induced by electron–phonon interactions, which induce local lattice distortions [25–29] and result in trapping of the charge carriers. In conventional semiconductors such as Si and GaAs, the effect of lattice distortion is typically neglected as the mobility of charge carriers can be described by classical movement inside the energy bands. In case of charge trapping, occupation of a trap occurs once the Fermi level crosses a certain level, which is denominated as charge transition level of the traps, E_T^e for electrons and as E_T^h for holes. These charge transition levels constitute upper and lower limits of the Fermi level, E_F [7]. The energy difference between the charge transition levels of electron and hole traps hence defines the *transport gap* of the material: $E_g^{tr} = E_T^e - E_T^h$. The transport gap is directly relevant for photo-electric and photo-catalytic applications. For the former, the splitting of the quasi Fermi levels, which determines the photovoltage of a device [30], is limited by the transport gap. For photocatalytic processes, the charge transfer at the active interface occurs from the trap levels of the solid and not from the band edge energies [31]. The latter explains the poor efficiency of Fe_2O_3 for solar water splitting despite an apparently ideal energy gap of 2.2 eV, where electron trapping limits the Fermi level to values of $E_{CB} - E_F > 0.5\,\text{eV}$ [32].

The transport is determined by non-interacting trapped electrons and holes and has thus to be distinguished from the energy gap measured by optical transitions, the *optical energy gap*, E_g^{opt}, where Coulomb attraction between electrons and holes can result in the formation of bound electron–hole pairs, so-called excitons. The exciton binding energies in conventional semiconductors are typically a few meV and therefore only noticeable at cryogenic temperatures, where they show up as narrow absorption peaks at photon energies slightly below the fundamental gap [2]. ZnO exhibits a slightly higher exciton binding energy of 59 meV, which can be observed at room temperature [33]. Excitonic absorption features are also pronounced in layered transition metal di-chalcogenides [34].

Due to the high permittivity of ferroelectrics, there is a strong tendency for the localization of charge carriers and the formation of polarons in ferroelectrics [26], since the large dielectric response of polar oxides reflects strong coupling between electronic charges and lattice polarization. This coupling allows local lattice distortions to effectively screen the carrier's Coulomb potential, lowering its self-energy and

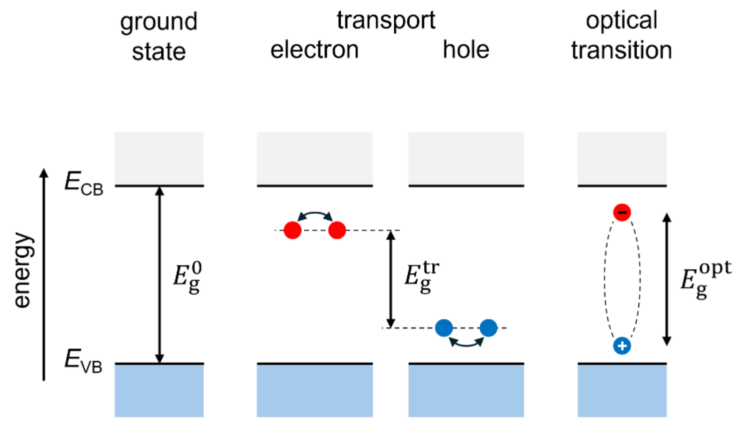

Figure 3. Schematic comparison of the fundamental gap (E_g^0), corresponding to the ground state energy difference of the valence band maximum and the conduction band minimum, the transport gap (E_g^{tr}) emerging from charge trapping and the optical gap (E_g^{opt}), related to exciton formation, of ferroelectrics. The curved solid lines with arrows indicate hopping transport while the curved dashed lines indicate the Coulomb attraction of the photo-excited electron–hole pair forming an exciton. The order of the magnitudes of the different energy gaps, $E_g^0 > E_g^{opt} > E_g^{tr}$, follows the experimental observations described in this work.

stabilizing a localized state [27, 28]. Examples include hole polarons at oxygen sites in $BaTiO_3$ [12, 35, 36], $LiNbO_3$ [11, 12, 37] and $KTaO_3$ [8], hole polarons at Pb-sites in $Pb(Zr,Ti)O_3$ [9], electron polarons on Ti sites in $Pb(Zr,Ti)O_3$ [9, 38] and Nb-sites in $LiNbO_3$ [11]. Although the existence of polarons has been reported, the experimental determination of trapping energies and transport gaps is largely missing and often misinterpreted using the activation energies determined from, e.g. temperature dependent electric conductivity. Also exciton formation is known for ferroelectrics and considerable exciton binding energies of ≈ 1 eV were reported in literature for $LiNbO_3$ [37], $KNbO_3$ [39] and $NaNbO_3$ [40]. A tentative scheme for the three different energy gaps in ferroelectrics is depicted in figure 3.

The distinction between the fundamental, transport and optical energy gaps is well-known for organic semiconductors, where excess charges are localized on small molecules or molecular units of larger molecules (polymers) [41, 42]. The occupation of non- or anti-bonding orbitals (lowest unoccupied molecular orbital) by an electron or the removal of an electron from the highest occupied molecular orbital results in a strong electronic polarization of the molecule and in a distortion of the chemical bonds associated with a structural relaxation. Trapping energies in organic molecules are naturally high with magnitudes up to few hundred meV. For the same reason, exciton binding energies in organic semiconductors are up to 1.5 eV depending on the size of the molecules [42, 43]. In organic semiconductors, the order of the energy gaps is $E_g^0 > E_g^{tr} > E_g^{opt}$, which is different from the order anticipated in figure 3.

1.3. Ingredients for the determination of the energy gaps

While the determination of the optical gap by means of optical or electron spectroscopies for ferroelectrics is the same as for all materials, this work will demonstrate how the fundamental and transport gaps of ferroelectrics can be determined experimentally by a combination of x-ray photoelectron spectroscopy (XPS) and electrical transport measurements. The determination of the gaps is exemplified for two compounds exhibiting polaronic electronic conduction of both electrons and holes: $NaNbO_3$ and $0.94(Na_{0.5}Bi_{0.5})TiO_3$–$0.06BaTiO_3$ (NBT-6BT). Key ingredients enabling the determination of the fundamental and transport gap are in both cases (i) the direct determination of the charge transition level of either the electron or the hole polaron by means of XPS measurements [44–48]; (ii) the derivation of the position of the valence or conduction band edge relative to the trap level from the activation energy of electronic conductivity in an extrinsic temperature regime with fixed polaron concentration; (iii) the derivation of the Fermi level position in a temperature regime with temperature dependent polaron concentration from the activation energy of electronic conductivity; (iv) the determination of the trapping energy of the other polaron parameters from the activation energies of electronic conduction of a sample exhibiting a transition from n- to p-type behavior at a certain temperature.

The approach requires samples of the same material with different types of electronic conduction, i.e. effectively donor-doped and effectively acceptor-doped materials. Acceptor-doping often results in the formation of oxygen vacancies and the occurrence of oxygen ion conduction. This is particularly the case for NBT-based materials, where oxygen ion conduction dominates over (p-type) electronic conduction in effectively acceptor-doped compositions [49–53]. As the determination of the energy gaps requires the analysis of the electronic conduction, it is mandatory to discriminate between electronic and ionic conduction. In this work, electronic conduction is determined by means of direct current (DC) measurements. While alternating current (AC, impedance) measurements reveal the total conductivity (electronic + ionic), DC measurements can selectively probe electronic conductivity if the metal electrodes block ionic conduction (such as gold, silver and platinum) [54]. It is also mentioned that the frequency response of trapped charge carriers can be comparable to that of ions, while free electrons/holes react much faster to electric fields. The comparison of AC and DC conduction and the extraction of electronic conductivity for NBT-6BT is described in [55] and for $NaNbO_3$ in [56]. The separation between n- and p-type electronic conduction in $(Na_{0.5}Bi_{0.5})TiO_3$-based compositions is achieved by variation of the sample composition, as demonstrated by Sinclair and coworkers [49–51]. For $NaNbO_3$, the variation is accomplished by a comparison between nominally undoped and donor- (Ca-) doped samples.

The following of the article is organized as follows: section 2 provides details of sample preparation and characterization and of density functional theory calculations, which are performed to compare the fundamental band gap with those derived from experiments. The model used to extract the trap levels from the electrical conductivity measurements is outlined in section 3. Results obtained from optical, XPS and electrical measurements are described in sections 4–6, respectively. The extraction of polaron binding and formation energies is treated in section 7, eventually resulting in the experimental determination of the transport and fundamental gaps in section 8 and a confirmation of the fundamental gaps by density functional theory calculations in section 9. Finally, section 10 revisits the semiconducting nature of ferroelectric materials in the context of the presented results and sketches some consequences for material properties and for other ferroelectric compounds.

2. Methods

2.1. Sample preparation

$Na_{0.5}Bi_{0.5}TiO_3$–6$BaTiO_3$ (NBT-6BT): $0.94(Na_{0.5}Bi_{0.5})TiO_3$–$0.06BaTiO_3$ (NBT-6BT) and $0.94(Na_{0.51}Bi_{0.49})TiO_3$–0.06BT were prepared by solid-state synthesis. These samples will be marked as 50/50 and 51/49, respectively. Powders with given purities were utilized: Na_2CO_3 (99.95%), $BaCO_3$ (99.95%), Bi_2O_3 (99.975%) (all from Alfa Aesar GmbH & Co. KG, Germany) and TiO_2 (99.8%, Sigma Aldrich). After weighing the precursors as per the stoichiometry, the powders were milled with yttria-stabilized zirconia balls in ethanol for 4 h at 250 rpm, then dried and homogenized, and finally calcined at 900 °C for 3 h using a heating rate of 5 °C min^{-1}. Milling was subsequently repeated under the same conditions and was followed by one more drying step. Disk samples of 13 mm in diameter were pressed at a uniaxial pressure of 15.4 MPa, followed by an isostatic pressure of 300 MPa. The samples were placed in a closed alumina crucible with sacrificial powder and were sintered at 1150 °C for 3 h using a ramp rate of 5 °C min^{-1}. Crystal structure analyzed by x-ray diffraction, microstructure analyzed by SEM, and temperature as well as frequency dependent dielectric properties compare well with those reported previously [57–59]. The electrical properties of the samples, including temperature dependent DC and AC conductivities, are described in [55]. Only AC conductivities can be compared with literature, but correspond well with those reported in [59].

$NaNbO_3$: The polycrystalline undoped $NaNbO_3$ (NN) and Ca-doped $NaNbO_3$ (CaNN) samples were also prepared by solid-state reaction. Na_2CO_3 (99.9%, ChemPur) and orthorhombic Nb_2O_5 (99.9%, Sigma-Aldrich) powder were used as starting materials, with calcium carbonate ($CaCO_3$, 99.95%, Alfa Aesar) added for doping. Before mixing, the powders were milled first by attrition milling with isopropanol and yttria-stabilized zirconia balls for 2 h at 500 rpm in case of Nb_2O_5 and by planetary ball milling with acetone and yttria-stabilized zirconia balls for 4 h at 200 rpm for Na_2CO_3 and $CaCO_3$. Then the powders were dried at 100 °C for 1 h and at 200 °C for 2 h, sieved, and dried again at 100 °C for 2 h. The dried powders were weighed in a Labmaster 130 glove box (MBraun, Garching, Germany), mixed, and homogenized for 4 h. In case of the doped samples, $Na_{0.99}Ca_{0.01}NbO_3$ (CaNN), $CaCO_3$ was added according to a 1 mol% doping. The homogenization and all following milling steps were done with acetone and yttria-stabilized zirconia balls via planetary ball milling followed by drying at 105 °C for 1 h and at 200 °C for 2 h, sieving, and drying at 200 °C for 2 h. After homogenization, the powders were uniaxially pressed to pellets and calcined for 4 h at 700°C in case of $NaNbO_3$ in an alumina crucible. For $Na_{0.99}Ca_{0.01}NbO_3$, a calcination temperature of 950 °C was chosen. A second calcination step was performed at the same conditions after crushing the samples and milling them again for 3 h. After the final milling process for 3 h, pellets with a diameter of 8 mm were pressed isostatically with 200 MPa and sintered in air for 2 h at 1250 °C in case of pure and at 1320 °C for Ca-doped $NaNbO_3$. X-ray diffraction, microstructure, temperature dependent permittivity and conductivity, as well as room temperature polarization hysteresis loops of the studied samples are available at [40, 56]. The data agree well with literature reports [60–62].

2.2. Electrical conductivity measurements

NBT-6BT: The ceramic pellets were initially ground with sandpaper to achieve a thickness of 0.30–0.35 mm and then cut into small square-shaped pieces (length = 3.0 mm). To reduce the residual stress from grinding, the pellets were annealed at 450 °C for 1 h, with heating and cooling rates of 5 °C min^{-1} in a box furnace. Platinum (Pt) electrodes were then sputtered onto both sides of each pellet using a Quorum Q300T D sputter coater (Quorum Technologies Ltd., UK). The Pt electrodes were round shaped with a diameter of 2.5 mm for all samples.

The dynamic temperature dependence of conductivity was probed by the DC method in different atmospheres (dry air and N_2 with oxygen partial pressures of 10^5 and 10^0, respectively): the sample was ramped up at a constant rate of 2.5 °C min^{-1} to 450 °C, held at 450 °C for one hour, and then cooled back to room temperature at the same rate. During this thermal cycling, a fixed DC voltage of 0.5 V using a Keithley 6487 picoammeter (Tektronix, Inc. USA) was continuously applied, and the current through the sample was recorded. This thermal cycling was performed twice to check reproducibility. The oxygen partial pressure was monitored using the SGM5-EL electrolysis device (ZIROX Sensoren & Elektronik GmbH, Germany).

$NaNbO_3$: The densified samples were ground to a thickness of 0.7 mm. Platinum electrodes were sputtered on the surfaces. The dynamic temperature dependence of conductivity were also recorded by the DC method in different atmospheres (dry air and N_2 with oxygen partial pressures of 10^5 and 10^0, respectively): the sample was ramped up at a constant rate of 1.0 °C min^{-1} to 500 °C or 600 °C, held for 2 min, and then cooled back to room temperature at the same rate. During this thermal cycling, a fixed DC voltage of 0.1 V or 1.0 V was applied.

2.3. XPS

NBT-6BT: *in situ* XPS: the sintered ceramic samples were first ground with sandpaper (#800, #1200) to 0.45 mm thickness and then cut into a rectangular shape of 3×4 mm^2. The samples were subsequently annealed in air at 450 °C for 1 h to relieve the residual stress introduced by machining. The bottom electrodes of Pt with a thickness of 50 nm were deposited with a sputter coater (Quorum Q300T D, Quorum Technologies Ltd., UK). Before the deposition of the indium tin oxide (ITO) top electrode, a surface cleaning was carried out inside the deposition chamber of the Darmstadt Integrated System for Materials Research by heating in oxygen (0.5 Pa, 400 °C, 0.5 h) to remove adventitious carbon species. Top electrodes of 10% Sn-doped In_2O_3 with a thickness of 2 nm were subsequently deposited by radio frequency (RF) magnetron sputtering either at room temperature for subsequent annealing or at 400 °C. Finally, the samples were mounted onto stainless-steel sample holders allowing for separate electrical contacts to the bottom and top electrode. The ITO electrode was connected to the ground, ensuring that the Fermi energy at the top of the sample is aligned with that of the spectrometer, which serves as a binding energy reference for the spectra. XPS measurements were then executed by a Physical Electronics PHI 5700 spectrometer system (Chanhassen, MN) with monochromated Al Kα radiation. Binding energies were calibrated using a sputter cleaned Ag foil. XPS measurements were performed either in the course of heating the samples inside the XPS chamber or by applying a positive voltage to the Pt electrode at elevated temperatures.

$NaNbO_3$: For the interface experiment, the clean surfaces were first characterized in the analysis chamber using XPS. The electrode material was then deposited stepwise with increasing thickness until the substrate signals were attenuated, with XPS measurements performed after each deposition step. ITO was deposited via RF magnetron sputtering at a power of 25 W under an Ar flow of 10 sccm and a pressure of 0.5 Pa at 400 °C, resulting in a sputter rate of 5 nm min^{-1} and a polycrystalline film. For RuO_2 deposition, DC magnetron sputtering at room temperature was used to grow amorphous RuO_2 on the sample surface. The sputtering conditions were 10 W power and 1 Pa pressure in an Ar/O_2 mixture (9.25 sccm Ar and 0.75 sccm O_2), yielding a sputter rate of 3 nm min^{-1}. XPS analysis was performed using a Physical Electronics PHI 5700 spectrometer (Physical Electronics, Chanhassen, MN) with monochromatic Al Kα excitation. All spectra were calibrated using a sputter-cleaned Ag foil, with the Fermi edge set to 0 eV.

2.4. Optical measurements

NBT-6BT: The optical band gap (E_g) of NBT-6BT was determined from DR spectra of powder samples recorded with a Shimadzu UV-2600i over the wavelength range of 220–1400 nm.

$NaNbO_3$: Low-loss electron-energy loss measurements (EELS) spectra were acquired using the Zeiss SESAM microscope (ZEISS GmbH, Wetzlar, Germany) at an acceleration voltage of 200 kV in TEM mode. The microscope is equipped with an electrostatic Ω-type monochromator (CEOS GmbH, Heidelberg, Germany) and the in-column MANDOLINE energy filter. EELS data were acquired with an energy resolution of 60 meV, as determined from the full width at half-maximum of the zero-loss peak.

2.5. Density functional theory calculations

NBT: All calculations were performed with the Vienna *ab initio* simulation package (VASP) [63–66] using the projector-augmented-wave (PAW) method [67, 68]. Band gaps of NBT were computed within the GW approximation [69]. For Brillouin-zone sampling, we used Monkhorst-Pack k-point meshes with the density of approximately 27 Å and 22 Å for 100- and 111-ordered structures, respectively. The primitive cells for 100- and 111-ordered structures contained 20 and 10 atoms, respectively. Ionic coordinates and cell parameters were relaxed at the DFT level until the residual forces on atoms were less than 0.02 eV Å^{-1}. PBEsol exchange-correlation functional [70] was used. A planewave cutoff of 700 eV was used which ensures the total energy to be converged to 1 meV/atom. Standard PAW datasets supplied with VASP were employed [67, 68]. The valence configurations were Bi: $5d^{10}6s^26p^3$, Na: $2s^22p^63s^1$, Ti: $3s^23p^63d^34s^1$, and O: $2s^22p^4$.

Starting from the relaxed structures and DFT wavefunctions, quasiparticle band gaps were obtained from single-shot G_0W_0 calculations, as implemented in VASP [71–74]. We used the GW-optimized PAW datasets distributed with VASP. The corresponding valence configurations were Bi: $5s^25d^{10}6s^26p^3$, Na: $2s^22p^63s^1$, Ti: $3s^23p^63d^4$, and O: $2s^22p^4$. Workflow execution was automated with atomate2 [75].

$NaNbO_3$: For orthorhombic $NaNbO_3$ (Pbcm), the experimental CIF [76] was used as the starting structure (lattice parameters $a = 5.50$ Å, $b = 5.56$ Å, $c = 15.54$ Å; $\alpha = \beta = \gamma = 90^\circ$). The structure was relaxed at the DFT level using the same exchange–correlation functional, plane-wave cutoff, and force-convergence threshold as described above, with a Monkhorst–Pack $10 \times 10 \times 4$ **k**-point mesh. A 40-atom primitive cell was employed. The optimized lattice constants are $a = 5.49$ Å, $b = 5.55$ Å, and $c = 15.43$ Å, with $\alpha = \beta = \gamma = 90^\circ$, which are in good agreement with experiment. The PAW pseudopotentials were employed for both the DFT geometry optimization and the *GW* calculations, using Na $2s^2\,2p^6\,3s^1$, Nb $4s^2\,4p^6\,4d^4\,5s^1$, and O $2s^2\,2p^4$ valence configurations. Quasiparticle band gaps were obtained from single-shot G_0W_0 calculations using a $4 \times 4 \times 2$ **k**-point mesh.

3. Polaron conduction

Depending on the type of polarons present, electrical conduction can occur via small or large polaron transport [25–29]. In this work, we focus on small polaron conduction, which is considered the more likely mechanism in NBT and NN systems.

Small polaron conduction involves the thermally activated hopping of a localized charge carrier, either an electron or a hole, from one trapping site to an adjacent site. This process is illustrated in figure 4(a), where two potential wells represent neighboring sites. For a carrier to hop from site 1 to site 2, the carrier must overcome the energy barrier separating the wells.

Polaron transport can occur in two distinct regimes: adiabatic and non-adiabatic (diabatic). In the adiabatic regime, typically relevant at low temperatures (e.g. when cooling from room temperature to 20 K), the charge hopping frequency exceeds the phonon frequency. This allows for tunneling between sites due to significant orbital overlap, characterized by the electronic coupling strength V_{12} (see figure 4(a)). In contrast, the diabatic regime, dominant at high temperatures (e.g. when heating from room temperature to several hundred degrees Celsius), features weaker orbital overlap due to phonon, induced lattice vibrations, reducing the tunneling probability. As a result, the activation energy required for hopping is effectively higher in the diabatic case than in the adiabatic case, with the difference roughly corresponding to V_{12}.

In general, the electrical conductivity due to polaron transport can be expressed as follows:

$$\sigma = \frac{\sigma_0}{T^A}\exp\left(-\frac{E_a}{k_B T}\right). \tag{2}$$

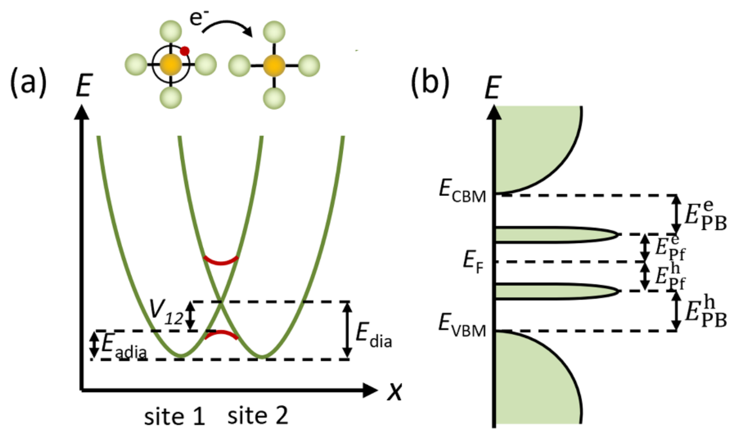

Figure 4. (a) Polaron hopping between two adjacent sites for the adiabatic and diabatic cases, characterized by activation energies E_{adia} and E_{dia}, respectively (inspired by [25]). V_{12} denotes the electronic coupling strength. (b) Schematic band structure showing a hole and an electron polaron band, with polaron binding energy E_{PB} and polaron formation energy E_{Pf} (inspired by [77]).

The exponent A in the prefactor equals 1 in the adiabatic regime and $\frac{3}{2}$ in the diabatic regime. The polaron concentration c_{p} and mobility μ_{p} are given by equations:

$$\begin{aligned} c_{\text{p}} &= N_{\text{p}} \exp\left(-\frac{E_{\text{Pf}}}{k_{\text{B}}T}\right) \\ \mu_{\text{p}} &= \frac{\mu_0}{T^A} \exp\left(-\frac{E_{\text{(a)dia}}}{k_{\text{B}}T}\right). \end{aligned} \tag{3}$$

Here, N_{p} denotes the number of available polaron sites, and E_{Pf} represents the polaron formation energy, defined as the energetic difference between the polaron level and the Fermi level E_{F}. Figure 4(b) illustrates the formation energies for both hole and electron polarons. Additionally, the polaron binding energy E_{PB} is indicated, which corresponds to the energy difference between the polaron level and the VBM for a hole polaron, or the CBM for an electron polaron. The relationship between the polaron binding energy and the (a)diabatic activation energy is given by:

$$\begin{aligned} E_{\text{PB}} &= 2\left(E_{\text{adia}} + V_{12}\right) && \text{adiabatic regime} \\ E_{\text{PB}} &= 2E_{\text{adia}} && \text{diabatic regime.} \end{aligned} \tag{4}$$

Accordingly, the overall activation energy E_{A} for polaron conductivity can be expressed as:

$$\begin{aligned} E_{\text{A}} &= E_{\text{Pf}} + E_{\text{adia}} = E_{\text{Pf}} + \frac{E_{\text{PB}}}{2} - V_{12} && \text{adiabatic regime} \\ E_{\text{A}} &= E_{\text{Pf}} + E_{\text{adia}} = E_{\text{Pf}} + \frac{E_{\text{PB}}}{2} && \text{diabatic regime.} \end{aligned} \tag{5}$$

In this work, the analysis is restricted to the diabatic regime, which aligns with the employed conductivity measurements in the range between room temperature and 450 °C–600 °C.

Typical Arrhenius plots are obtained using the product of the conductivity and $T^{3/2}$ as a function of $1000/T$, as shown in figure 5, which displays two regimes: extrinsic and 'intrinsic'. The extrinsic regime refers to a temperature range where the polaron concentration is fixed by external factors such as dopants or other defects. Under these conditions, the activation energy corresponds to half of the polaron binding energy:

$$\begin{aligned} \sigma_{\text{ext}} &= c_{\text{p}} \cdot \mu_{\text{p}} \cdot q \\ &= c_{\text{p,ext}} \cdot \frac{\mu_0}{T^{3/2}} \exp\left(-\frac{E_{\text{PB}}}{2k_{\text{B}}T}\right) \cdot q \\ &= \frac{\sigma_0}{T^{3/2}} \exp\left(-\frac{E_{\text{PB}}}{2k_{\text{B}}T}\right) \Rightarrow E_{\text{A,ext}} = \frac{E^{\text{e/h}}_{\text{PB}}}{2}. \end{aligned} \tag{6}$$

The 'intrinsic' regime, by contrast, occurs at higher temperatures where sufficient thermal energy is available to overcome the polaron (transport) gap, $E^{\text{e}}_{\text{Pf}} + E^{\text{h}}_{\text{Pf}}$, leading to dominant intrinsic polaron conduction. Here, the activation energy accounts for both the formation energy of the polarons and half of

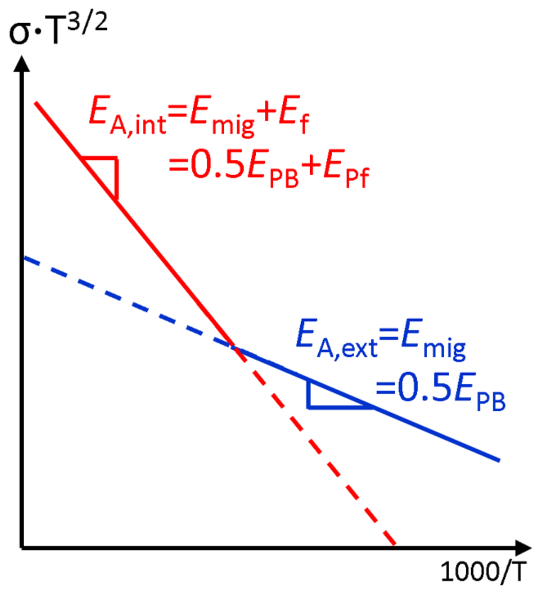

Figure 5. Identification of the extrinsic (blue) and 'intrinsic' (red) regimes from the plot of $\sigma \cdot T^{3/2}$ as a function of $1000/T$.

their binding energy:

$$\begin{aligned}\sigma_{\text{int}} &= c_{\text{p}} \cdot \mu_{\text{p}} \cdot q \\ &= N_{\text{p}} \exp\left(-\frac{E_{\text{Pf}}}{k_{\text{B}}T}\right) \cdot \frac{\mu_0}{T^{3/2}} \exp\left(-\frac{E_{\text{PB}}}{2k_{\text{B}}T}\right) \cdot q \\ &= \frac{\sigma_0}{T^{3/2}} \exp\left(-\frac{E_{\text{Pf}} + \frac{E_{\text{PB}}}{2}}{k_{\text{B}}T}\right) \Rightarrow E_{\text{A,int}} = \frac{E_{\text{PB}}^{\text{e/h}}}{2} + E_{\text{Pf}}^{\text{e/h}}.\end{aligned} \tag{7}$$

4. Optical transitions

4.1. NBT-6BT

The optical band gap was determined from DR measurements using Tauc's equation [78, 79],

$$(\alpha h\nu) = C\left(h\nu - E_{\text{g}}\right)^{q} \tag{8}$$

where α is the absorption coefficient, h is Planck's constant (4.135×10^{-15} eV·s), ν is photon's frequency (s^{-1}), $h\nu$ is incident photon energy, C is a constant, E_{g} is the optical band gap, and q is an exponent that depends on the nature of the electronic transition, with $q = 1/2$ for direct allowed transitions and $q = 2$ for indirect allowed transitions [22]. In a direct transition, the electron moves from the valence band to the conduction band without a change in crystal momentum, so photon absorption alone provides the required energy (as in GaAs or $BaTiO_3$). In contrast, an indirect transition requires a simultaneous phonon interaction to conserve momentum, as in Si or $SrTiO_3$ [2, 80].

For DR measurements, a Tauc plot was constructed by replacing the absorption coefficient α with the Kubelka–Munk function $F(R_\infty)$, which transforms the raw reflectance data into an equivalent absorption spectrum. The Kubelka–Munk function is defined as [81, 82]:

$$\alpha = F(R_\infty) = \frac{K}{S} = \frac{(1 - R_\infty)^2}{2R_\infty} \tag{9}$$

where $F(R_\infty)$ is the K–M function, K and S are the absorption and scattering coefficients, respectively, and R_∞ is the reflectance of an optically thick sample relative to that of a reference material [83].

Figures 6(a) and (b) show the Tauc plots assuming direct and indirect allowed transitions, respectively, where $(\alpha h\nu)^2$ and $(\alpha h\nu)^{1/2}$ are plotted as a function of the incident photon energy. The optical band gaps, estimated from the intersection of the linear portion of the curve with the photon energy axis, are approximately 3.45 eV and 3.25 eV, respectively.

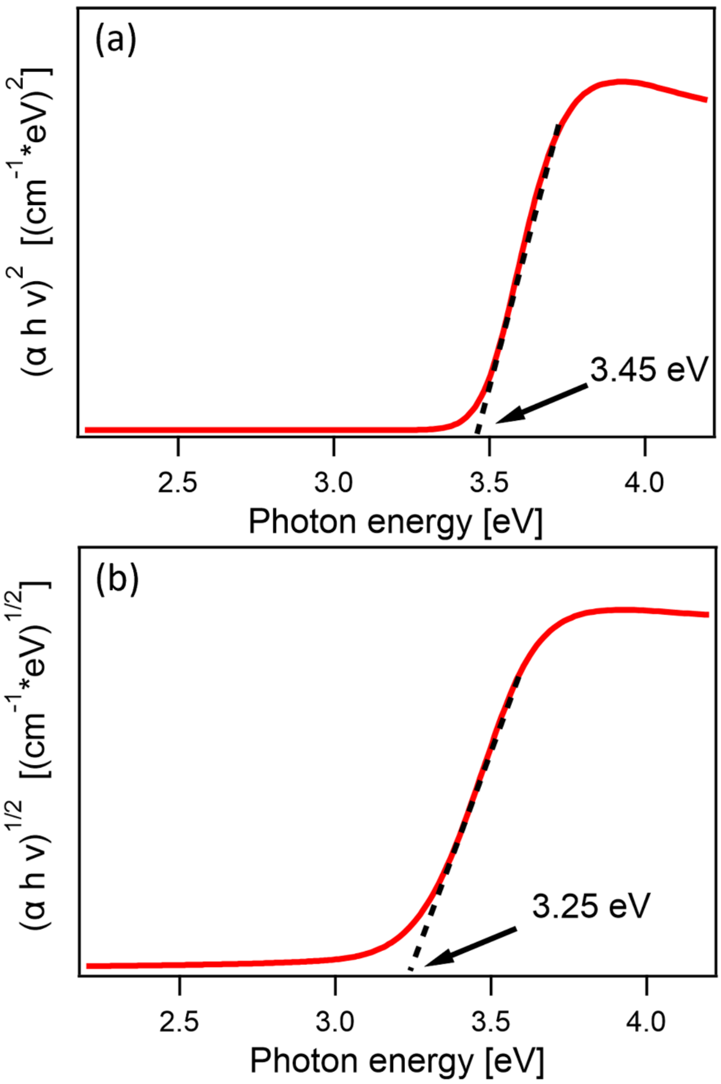

Figure 6. Tauc plots of NBT-6BT for (a) representation for a direct allowed transition: $(\alpha h\nu)^2 = f(h\nu)$ and (b) for an indirect allowed transition: $(\alpha h\nu)^{1/2} = f(h\nu)$.

4.2. $NaNbO_3$

Bein *et al* employed EELS in a transmission electron microscope to determine the optical band gap of $NaNbO_3$ and donor (Sr) doped $NaNbO_3$ [40]. Both samples exhibit well-defined absorption edges with band gaps of 3.53 eV, which are in very good agreement with values of 3.4–3.5 eV obtained from optical spectroscopy reported in literature [84–87].

5. XPS

The XPS analyses used in this work have already been reported elsewhere [40, 46].

5.1. NBT-6BT

The electron-trapped level in NBT-6BT was determined using *in-situ* XPS. Polycrystalline bulk ceramic samples were coated with 2–3 nm thick layers of 10% Sn-doped In_2O_3 (ITO). When a positive voltage was applied from the bottom Pt electrode across the cell, cathodic polarization of the ITO electrode attracted oxygen vacancies, leading to a reduction of the ITO. Metallic Bi was detected when the Fermi energy at the NBT-6BT surface increased to $E_F - E_{VB} = 2.47 \pm 0.10$ eV, indicating that the electron-trapped level is associated with the $Bi^{3+/0}$ charge transition level and corresponds to $E_F - E_{VB} = 2.47 \pm 0.10$ eV (as shown in figure 7(a)) [46].

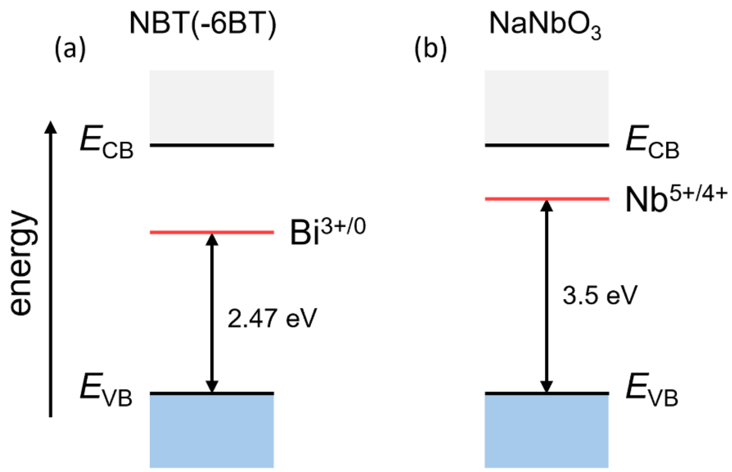

Figure 7. The upper limit of the Fermi level, corresponding to the energy distance between the electron trap level and the valence band maximum (VBM) in NBT-6BT [46] and $NaNbO_3$ [40]. The electron trap sites are associated with the $Bi^{3+/0}$ in NBT-6BT [46] and the $Nb^{5+/4+}$ in $NaNbO_3$ [88–90].

5.2. $NaNbO_3$

The band gap of $NaNbO_3$ should be larger than the 3.4–3.5 eV range reported in the literature based on optical spectroscopy and EELS [40]. This conclusion is supported by *in situ* XPS and electrical conductivity measurements. Specifically, the VBM of $NaNbO_3$ was determined from Schottky barrier heights at interfaces with low-work function Sn-doped In_2O_3 and high-work function RuO_2, using XPS with *in situ* interface preparation. The results indicate that the valence-band edge of $NaNbO_3$ is comparable to those of $SrTiO_3$ and $BaTiO_3$. Considering that $SrTiO_3$ and $BaTiO_3$ have band gaps of approximately 3.2 eV, close to the 3.4–3.5 eV values previously reported for $NaNbO_3$, the CBM of $NaNbO_3$ is expected to be at a similar energy level. Based on this band alignment, donor doping would be expected to produce electrical conductivities on the order of 1 $S\,cm^{-1}$, similar to donor-doped $SrTiO_3$ and $BaTiO_3$. In contrast, bulk ceramics of Sr- and Ca-doped $NaNbO_3$ exhibit room-temperature conductivities of only $10^{-10}\,S\,cm^{-1}$, barely higher than undoped $NaNbO_3$. Moreover, high-field conductivity and impedance spectroscopy show no evidence that this extremely low conductivity arises from insulating grain boundaries. Therefore, the band gap of $NaNbO_3$ should exceed 3.4–3.5 eV.

Moreover, the upper limit of the Fermi level, corresponding to the energy distance between the electron trap level and the VBM, was also determined to be 3.5 eV from the interface experiment between ITO and $NaNbO_3$ (as shown in figure 7(b)). It is noted that no noticeable amount of Nb^{4+} is detected in XPS [40]. The specific trapping site for electrons could thus not be identified directly. However, it is likely that electrons are trapped on Nb sites involving a $Nb^{5+/4+}$ valence change, as it is the case for $LiNbO_3$ [88–90]. In addition, hole polarons are also primarily assumed to be located at oxygen sites in this work [88, 90, 91].

6. Electrical transport measurements

6.1. NBT-6BT

Figures 8(a) and (b) show the product of the conductivity and $T^{3/2}$ plotted as a function of $1000/T$ for $Na_{0.51}Bi_{0.49}TiO_3$-6BT (51/49) and $Na_{0.50}Bi_{0.50}TiO_3$-6BT (50/50) samples. As seen in figure 8(a), the 51/49 sample exhibits p-type conduction across the whole temperature region, evidenced by its higher conductivity in dry air compared to N_2. The p-type conduction at high temperature is confirmed by oxygen partial pressure dependent conductivity measurements described in detail in [55]. An extrinsic region is observed at lower temperatures, with an activation energy (E_a) of 0.54 eV for both atmospheres, while the 'intrinsic' region at higher temperatures shows E_a values of 1.10 eV in dry air and 1.11 eV in N_2.

In contrast, the 50/50 sample (figure 8(b)) shows no clear extrinsic regime but only an 'intrinsic' region, making it difficult to determine the binding energy of trapped charges. However, a transition in the dominant carrier type is observed within this 'intrinsic' region near 320 °C, shifting from hole to electron polaron conduction, with E_a values of 1.39 eV in dry air and 1.56 eV in N_2. The sample showing the transition between n- and p-type conduction and the two different activation energies will be utilized later to determine the transport gap.

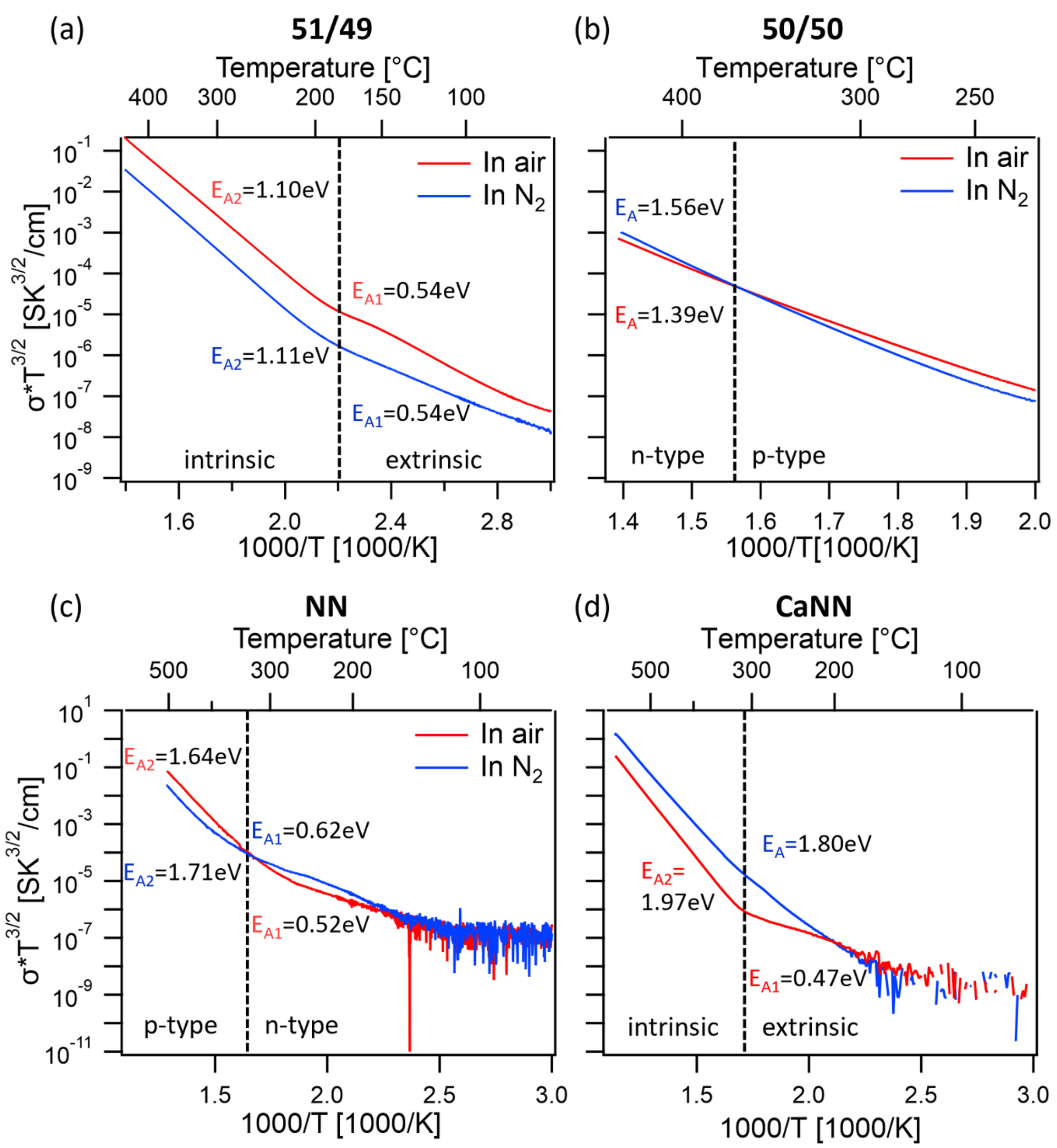

Figure 8. The product of the DC conductivity and $T^{3/2}$ as a function of $1000/T$ for (a) $Na_{0.51}Bi_{0.49}TiO_3$-6BT (51/49), (b) $Na_{0.50}Bi_{0.50}TiO_3$-6BT (50/50), (c) $NaNbO_3$ (NN) and (d) Ca-doped $NaNbO_3$ (CaNN).

6.2. $NaNbO_3$

Figures 8(c) and (d) show the product of conductivity and $T^{3/2}$ plotted as a function of $1000/T$ for NN and CaNN samples. The NN sample exhibits n-type conduction in the extrinsic region at lower temperatures and p-type conduction in the 'intrinsic' region at higher temperatures. The p-type nature of conduction at high temperature is confirmed by the change of conductivity upon a variation of the oxygen content in the gas atmosphere [56]. In contrast, the Ca-doped sample exhibits n-type conduction across the entire temperature range, with a pronounced extrinsic region in dry air. The average activation energy (E_a) in the extrinsic region for both samples is approximately 0.5 eV.

7. Polaron binding and formation energies

The fundamental and transport gaps of NBT-6BT and $NaNbO_3$ ceramics are now determined based on polaron conduction behavior observed in dynamic, temperature-dependent measurements combined with XPS analysis. To derive the gaps, the electron and hole polaron binding energies and formation energies (see figure 4) have to be extracted from the measurements.

Table 1. Hole and electron polaron concentration and mobility at 500 °C in air for $NaNbO_3$ and Ca-doped $NaNbO_3$.

	c_{O^-} (cm^{-2})	μ_{O^-} (cm^2 V^{-1} s^{-1})	$c_{Nb^{4+}}$ (cm^{-2})	$\mu_{Nb^{4+}}$ (cm^2 V^{-1} s^{-1})
NN	$4.24\cdot10^{12}$	4.15	$2.02\cdot10^{11}$	0.42
CaNN	$5.42\cdot10^{10}$	4.15	$4.05\cdot10^{12}$	0.42

7.1. NBT-6BT

The binding energy of trapped holes (E^{h}_{PB}) is twice the activation energy in the extrinsic region ($E^{p}_{a,ext}$) of the p-type 51/49 sample (figure 8(a)). It is derived as 1.08 eV.

In contrast, the binding energy of trapped electrons (E^{e}_{PB}) is determined indirectly from the n-type 50/50 sample (figure 8(b)). In this sample, a transition in the dominant carrier type is observed near 320 °C, shifting from hole to electron polaron conduction. From the p-type regime, the Fermi level position (E^{FL}_{VBM}) can be estimated using the formation energy of trapped holes (E^{h}_{Pf}):

$$\begin{aligned} E^{h}_{Pf} &= E^{p}_{a,int} - E^{h}_{PB} = 1.39 - \frac{1.08}{2} = 0.85\,\text{eV} \\ \triangle E^{FL}_{VBM} &= E^{h}_{Pf} + E^{h}_{PB} = 0.85 + 1.08 = 1.93\,\text{eV}. \end{aligned} \tag{10}$$

Given that the energy difference between the $Bi^{3+/0}$ trap level and VBM is 2.47 eV from the XPS measurement [46], the formation energy of trapped electrons (E^{e}_{Pf}) can be calculated as:

$$E^{e}_{Pf} = \triangle E^{Bi^{3+/0}}_{VBM} - E^{FL}_{VBM} = 2.47 - 1.93 = 0.54\,\text{eV}. \tag{11}$$

The binding energy for electron traps (E^{e}_{PB}) in the n-type 'intrinsic' region is then:

$$E^{e}_{PB} = 2\times\left(E^{e}_{a,int} - E^{e}_{Pf}\right) = 2\times(1.56 - 0.54) = 2.04\,\text{eV}. \tag{12}$$

7.2. $NaNbO_3$

Both NN and CaNN samples show n-type behavior in the extrinsic region (figure 8). The E^{e}_{PB} is taken to be twice the average activation energy in the extrinsic region ($E^{n}_{a,ext}$), giving a value of 1.0 eV (figure 9(b)). We then apply the equations derived in section 3 to simulate the conductivity. In the following we use Nb^{4+} and O^- to specify electron and hole traps, as Nb and O are the most likely trapping-sites in the niobates [88–91]. The calculations are, however, not specific for Nb and O, but are valid for any trapping site:

$$\begin{aligned} \text{NN:}\quad \sigma_{ext} &= c_{Nb^{4+}}\cdot\mu_{Nb^{4+}}\cdot q \\ &= \left[Nb'_{Nb}\right]_{ext}\cdot\frac{\mu_{Nb^{4+},0}}{T^{3/2}}\exp\left(\frac{E^{e}_{PB}/2}{k_B T}\right)\cdot q \\ \sigma_{int} &= c_{O^-}\cdot\mu_{O^-}\cdot q \\ &= N_O\exp\left(-\frac{E^{h}_{Pf}}{k_B T}\right)\cdot\frac{\mu_{O^-,0}}{T^{3/2}}\exp\left(\frac{E^{h}_{PB}/2}{k_B T}\right)\cdot q \\ \text{CaNN:}\quad \sigma_{ext} &= c_{Nb^{4+}}\cdot\mu_{Nb^{4+}}\cdot q \\ &= \left[Nb'_{Nb}\right]_{ext}\cdot\frac{\mu_{Nb^{4+},0}}{T^{3/2}}\exp\left(\frac{E^{e}_{PB}/2}{k_B T}\right)\cdot q \\ \sigma_{int} &= c_{Nb^{4+}}\cdot\mu_{Nb^{4+}}\cdot q \\ &= N_{Nb}\exp\left(-\frac{E^{e}_{Pf}}{k_B T}\right)\cdot\frac{\mu_{Nb^{4+},0}}{T^{3/2}}\exp\left(\frac{E^{e}_{PB}/2}{k_B T}\right)\cdot q. \end{aligned} \tag{13}$$

Figure 9 presents the measured and fitted conductivities of (a) $NaNbO_3$ and (b) Ca-doped $NaNbO_3$ in air, including all relevant energy parameters. The binding energy of trapped holes (E^{h}_{PB}) for CaNN was determined from the simulation parameters, as shown in table 1, to be no greater than 0.2 eV when fulfilling the condition that the binding and formation energies of hole polarons are adjusted such that the 'intrinsic' hole conductivity remains lower than the 'intrinsic' electron conductivity.

Subsequently, E^{e}_{Pf} and E^{h}_{Pf} for NN (figure 9(a)) were determined from the simulation parameters, also summarized in table 1, to be 1.76 eV and 1.54 eV, respectively.

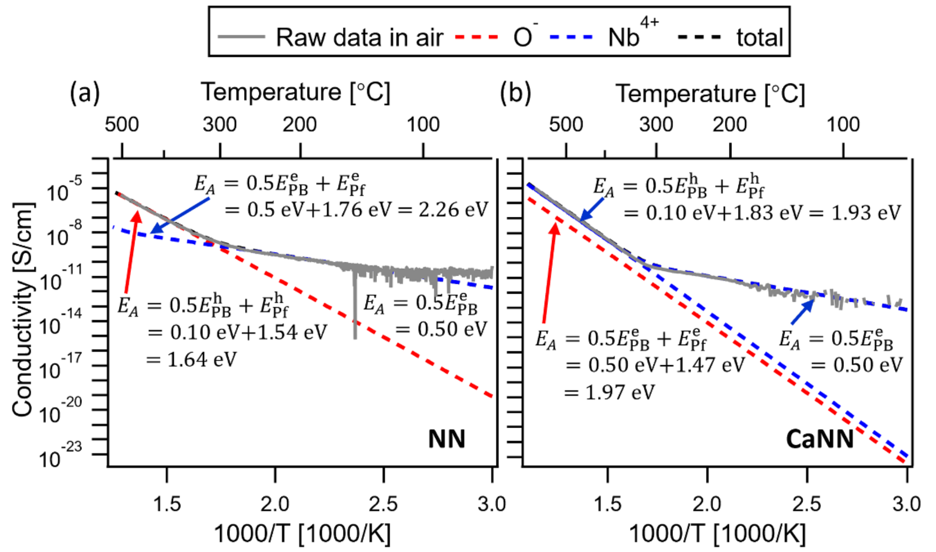

Figure 9. Measured and fitted conductivity of (a) $NaNbO_3$ and (b) Ca-doepd $NaNbO_3$ in air including all relevant energies.

Table 2. Polaron binding (E_{PB}) and formation (E_{Pf}) energies of electrons and holes derived from experiment. The transport gaps (E_g^{tr}) are the sums of the polaron formation energies and the fundamental gaps (E_g^0) are the sums of the binding and formation energies of trapped electron and holes. The Fermi level with respect to the valence band maximum corresponds to the sum of the binding and formation energy of the hole polarons.

	E^{e}_{PB} (eV)	E^{e}_{Pf} (eV)	E^{h}_{PB} (eV)	E^{h}_{Pf} (eV)	E_g^{tr} (eV)	E_g^0 (eV)
NBT-6BT (51/49)	2.04	0.83	1.08	0.56	1.39	4.51
NBT-6BT (50/50)	2.04	0.54	1.08	0.85	1.39	4.51
NN	1.0	1.79	0.2	1.51	3.3	4.5
CaNN	1.0	1.48	0.2	1.82	3.3	4.5

8. The transport and fundamental gaps

Table 2 summarizes the polaron binding and formation energies for NBT-6BT and NN. Based on these values, the transport band gaps (E_g^{tr}) for NBT-6BT and NN are determined from the sums of the electron and hole polaron formation energies (figure 4) as 1.39 eV and 3.3 eV, respectively. The fundamental gaps are the sums of the electron and hole polaron formation and binding energies and are 4.51 eV for NBT-6BT and 4.5 eV for $NaNbO_3$. The Fermi level positions relative to the VBM, which are derived from table 2 by the sums of the hole polaron formation and binding energy for the two different dopings differ by 0.29 eV for NBT-6BT and by 0.31 eV for $NaNbO_3$. In both case, the more n-type sample exhibits the higher Fermi level, as expected. The electronic band structures determined from these numbers for the more p-type undoped $NaNbO_3$ (NN) and the more n-type NBT-6BT (50/50) are depicted in figure 10.

9. DFT calculation of the fundamental gaps

In order to validate the energy gaps extracted from the measurements in table 2 by combining trapping levels extracted from the combination of XPS and conductivity data with activation energies for carrier transport, GW calculations are performed. Figures 11(a) and (b) depict the projected density of states (pDOS) for cubic $Na_{0.50}Bi_{0.50}TiO_3$ (NBT) with *A*-site (100) and (111) cation orderings. The two orderings have different total energies [92] but yield very similar density of states. In both cases the upper valence band is dominated by O 2*p* states that hybridize with Bi 6*s*; the Bi 6*s* weight at the very VBM is small, consistent with a lone-pair contribution deeper in the valence manifold [93]. Bi 6*p* states appear in the lower valence region and are prominent throughout the conduction band. The conduction-band minimum is primarily Ti 3*d* in character with an appreciable admixture of Bi 6*p*, while Na states contribute negligibly near the band edges. As for the fundamental band gaps, both cases show values of approximately 4.5 eV, in good agreement with the experimentally derived value.

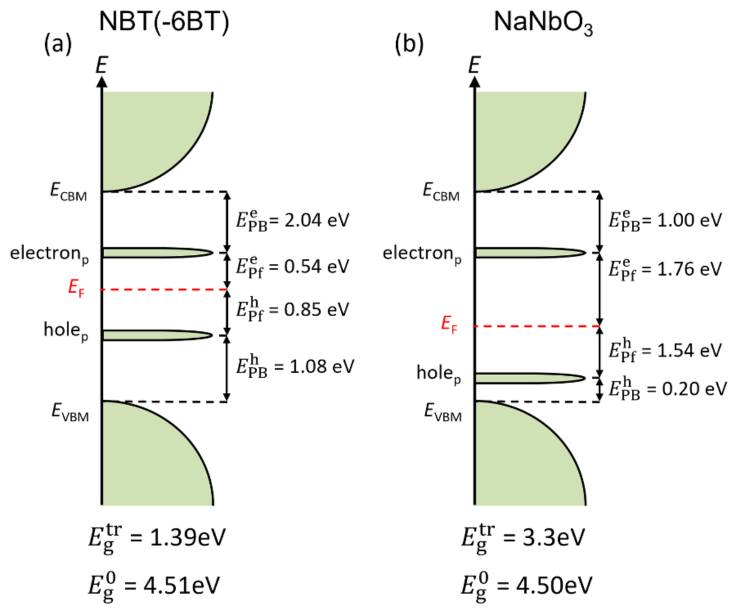

Figure 10. Schematic diagrams of the electronic band structures of (a) NBT-6BT (nominally stoichiometric 50/50) and (b) $NaNbO_3$ (nominally undoped NN) determined by electrical methods. In both cases, the binding energies and formation energies of trapped electrons and holes are indicated, along with the position of the Fermi level. The fundamental band gaps (E_g^0) of 4.51 eV and 4.50 eV are the sums of both polaron's binding and formation energies.

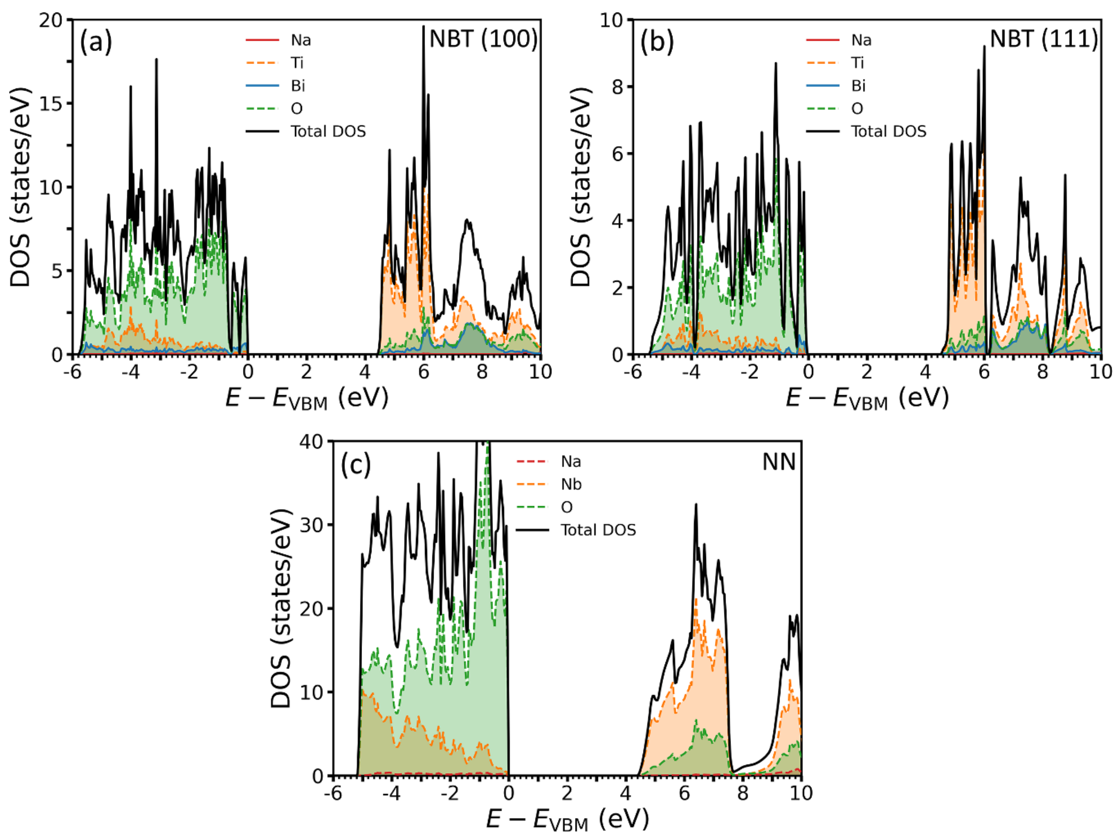

Figure 11. The projected density of states (pDOS) for cubic $Na_{0.5}Bi_{0.5}TiO_3$ with (a) (100) and (b) (111) *A*-site cation orderings and (c) $NaNbO_3$ calculated using density functional theory within the GW approximation. The different colors indicate the major orbital contributions to the electronic states.

Figure 11(c) presents the pDOS of orthorhombic $NaNbO_3$ computed with the same methodology. The valence band is largely O 2*p* in character with minor Nb 4*d* hybridization, and the conduction-band onset is dominated by Nb 4*d* states. Na contributions are weak away from the band edges. The fundamental band gap is approximately 4.40 eV, which is also in good agreement with the experimentally derived value. The fundamental gap of $NaNbO_3$ of 4.4–4.5 eV and its difference to the optical gap of 3.4–3.5 eV are also in good agreement with those of $LiNbO_3$ [37] and $KNbO_3$ [39].

Regarding the transport gaps, calculations should reveal the trapping energies of electrons and holes. While there has been significant progress in recent years regarding such calculations [26, 38], a quantitative agreement with experiment is still challenging. In the present case, the involvement of heavy elements, in particular Bi, will need additional efforts due to the requirement for relativistic treatments.

10. The semiconducting nature of ferroelectrics

The above results demonstrate that it is important to distinguish between different types of energy gaps when analyzing ferroelectric oxides. In organic semiconductors, the typical relationship follows: $E_g^0 > E_g^{tr} > E_g^{opt}$. In contrast, for the ferroelectric oxides studied here, the relationship is altered: $E_g^0 > E_g^{opt} > E_g^{tr}$ for NBT-6BT and NN, indicating that the optical gap lies above the transport gap, but below the fundamental gap.

The most important point to note is the presence of trapped charges, which substantially reduce the energy gap for charge transport. For NBT-6BT, the effect is so severe that the transport gap is only $1/3$ of the fundamental gap and less than $1/2$ of the optical gap. In an energy band diagram, the effect of trapped charges is best represented as shown in figures 2 and 3, using the fundamental gap for the position of the VBM and CBM and including the energetic positions of the trap levels. The different energy gaps have several consequences:

- Defect equilibria: The optical gap is irrelevant for the electronic defect equilibrium. The concentrations of free electrons and holes follows the fundamental gap and is thus very low, in most cases negligible. The concentration of trapped electrons and holes follows the transport gap and can be quite significant. A direct consequence of this is that the concentration of oxygen vacancies ($v_O^{\cdot\cdot}$) after sintering is not necessarily determined by the classical Schottky equilibrium with cation vacancies but may instead be constrained by the trapping of electronic carriers, such that $2[v_O^{2+}] = [e_{trap}^-]$. Similarly, cation vacancies can be coupled to trapped holes, leading to $n \times [v_{cat}^{n-}] = [h_{trap}^+]$ as dominant defect equilibrium.
- Energy gaps: the determination of an energy gap from the activation energy of electrical conductivity is not as straightforward as for classical semiconductors, as not only the carrier concentrations but also the carrier mobilities are thermally activated. The transport and the fundamental gap can both be determined using the evaluation described in this work. Such a determination requires more than one sample with varying type of electronic conduction and also other information, such as that provided by XPS analysis of a trapping level;
- Concentrations and mobilities of electronic carriers may be comparable to those of ionic carriers, making them more difficult to discriminate;
- Screening of polarization at charged domain walls and domain wall conductance are provided by trapped charges and not by free charges. This naturally explains the low conductivity of charged domain walls;
- Photovoltages in devices for photovoltaic energy conversion are limited by the transport gap, not by fundamental and not by optical gap;
- Charge transfer at interfaces for catalytic reactions involve the polaronic energy levels and not the fundamental VBM and CBM energies. This has as also been used to explain the low activity of Fe_2O_3 for hydrogen evolution [32];
- Except for $BaTiO_3$ and related compounds, DC leakage currents in bulk material are dominated by polaronic transport. It is mentioned that ionic currents can also contribute to AC leakage currents, e.g. during measuring polarization hysteresis loops;
- Injection of charge carriers upon applied electric field does not necessarily involve overcoming the Schottky barrier (which is still defined by the fundamental gap), but can occur directly by occupation of the trap levels as discussed in recent study of polarization screening at interfaces of antiferroelectric compounds [94];
- We expect that tunneling through thin ferroelectric films is not directly affected by the trap levels, but is governed by the barrier heights determined by the fundamental gap. However, any occupation of trap levels will affect the electrostatic potential, thereby affecting tunneling behavior as well.

It is further noted that the distinction into fundamental, optical and transport gaps is an intrinsic property of the materials, which occurs even in perfect single-crystalline entities. However, the magnitudes of the energy gaps can vary in real materials containing disorder and defects. A broadening of the fundamental gap (Urbach tails) may be induced, for example, by variation in local composition and/or strain [95]. The transport gap will be affected by defects, such as vacancies or dopants, via the formation of bound polarons likely having different trapping energies than self-trapped, free polarons. The interaction of excitons with defects or disordered regions in oxides might affect the optical gap, potentially causing a broadening or shift of the optically measured absorption edge. Trapped charges have also been observed at interfaces such as $(Ba,Sr)TiO_3/Al_2O_3$ interfaces, which can induce ferroelectric-like hysteresis loops of non-ferroelectric materials [96]. It remains unclear, whether these traps are the same as those occurring in bulk material other if they are specific to the interface is another issue remaining to be clarified.

The sequence of energy gaps is different from those reported for organic semiconductors. If exciton absorption would be a bound pair of a trapped electron and a trapped hole attracted by Coulombic forces, i.e. optical absorption proceeds via excitation of a pair of a trapped electron and hole, the optical gap should be equal or smaller than the transport gap. This is evidently not the case for the studied ferroelectrics, in agreement with calculations of exciton absorption in $LiNbO_3$ and $KNbO_3$ [37, 39], which do not take charge trapping into account. This indicates that trapping occurs subsequent to absorption on a time scale long enough to prevent a modification of the absorption edge. This is anticipated in figure 3, where the energy levels of the electrons and holes in the exciton are closer to the fundamental band edges than the energy levels of the trapped carriers.

Regarding different ferroelectric materials, barium titanate ($BaTiO_3$) represents a notable exception among ferroelectric oxides, as it does not exhibit significant electron trapping in the absence of oxygen vacancies [97] and trapped holes have very low trapping energies [12, 35, 36]. For this material, there is also no indication of significant differences between the fundamental, optical and electrical energy gaps. It has already been mentioned that polaronic charge carriers are also present in Pb-based piezoelectric oxides [9, 10, 45], involving Ti and Pb as trapping centers. Due to the higher VBM energy of the Pb-based perovskites compared to $SrTiO_3$ and $BaTiO_3$, hole trapping on oxygen is not expected [35, 98]. Whether the fundamental gap in Pb-based piezoelectrics is different from the optical gap remains unclear, but has to be expected. Another widely studied piezoelectric material is $BiFeO_3$, in which Fe is formally present as Fe^{3+}. As the small 3*d* orbitals particularly facilitate charge trapping, it is not surprising that both oxidation and reduction of Fe in $BiFeO_3$ have been reported [44, 99]. In particular, the upper limit of the Fermi level has been identified at $\approx 1.7\,eV$ above the VBM [44], indicating that the electronic gap is substantially smaller than the reported optical gap of 2.2–2.7 eV [100]. As for Pb-based compounds, the fundamental gap remains uncertain for $BiFeO_3$. With the noted exception for electron trapping in $BaTiO_3$, charge trapping and hence differences between the fundamental, optical and transport gaps are expected to be the rule in ferroelectric oxides, rather than the exception. They may also contribute to the properties of other ferroelectric wide gap materials, such as HfO_2 and AlScN.

11. Summary

In summary, this work underscores the necessity of distinguishing between the fundamental, optical, and electrical energy gaps in ferroelectric oxides, as each reflects distinct physical processes and electronic states. The fundamental gap represents the intrinsic ground-state separation between the valence and conduction bands, whereas the optical and transport gaps are governed by excited-state phenomena involving localized polaronic carriers. These differences, typically on the order of 1 electronvolt, have significant implications for interpreting the electronic and optoelectronic behavior of ferroelectrics. By combining optical spectroscopy, XPS, and conductivity measurements under controlled temperature and oxygen partial pressure, this study provides a comprehensive framework for determining and rationalizing these distinct energy gaps in NBT-6BT and $NaNbO_3$, demonstrating the hierarchy $E_g^0 > E_g^{opt} > E_g^{tr}$ in ferroelectric oxides. Additionally, DFT calculations within the GW approximation confirm the plausibility of a 4.5 eV fundamental band gap in NBT and $NaNbO_3$. Such insights lay a solid foundation for tailoring ferroelectric compounds toward emerging applications in energy conversion and catalytic devices.

Acknowledgment

The presented work has been executed within the collaborative research centre FLAIR (Fermi level engineering applied to oxide electroceramics), which is funded by the German Research Foundation (DFG), project-ID 463184206 – SFB 1548, and by the Austrian Fonds zur Förderung der wissenschaftlichen Forschung (FWF), Project Grant-DOI (10.55776/I6450). Additional support was provided by the state of Hesse, Germany, within the LOEWE priority project FLAME (Fermi Level Engineering of Antiferroelectric Materials for Energy Storage and High Voltage Insulation Systems), by the German

Academic Exchange Service (DAAD) through the PPP Slovenia, Project ID 57450108, and by the Slovenian Research Agency (core funding P2-0105 and bilateral Project No. BI-DE/19-20-008). Pengcheng Hu also acknowledges support from the China Scholarship Council (CSC), Award No. 202106220039. Paderborn supercomputing center is gratefully acknowledged by Mohammad Amirabbasi as the provider of needed computing facilities. Tadej Rojac and Barbara Malič gratefully acknowledge the financial support of the Slovenian Research and Innovation Agency (research core funding P2-0105). For the purpose of open access, the authors have applied a CC BY public copyright license to any Author Accepted Manuscript version arising from this submission.

Data availability statement

The data that support the findings of this study are openly available at the following URL/DOI: https://tudatalib.ulb.tu-darmstadt.de/handle/tudatalib/5034 [101].

Author contributions

Pengcheng Hu 0009-0005-2512-1321
Data curation (equal), Formal analysis (equal), Investigation (equal), Visualization (equal), Writing – original draft (lead), Writing – review & editing (equal)

Nicole Bein 0000-0003-3022-3283
Data curation (equal), Formal analysis (equal), Investigation (equal), Validation (equal), Visualization (supporting), Writing – review & editing (supporting)

Chinmay Chandan Parhi 0009-0004-2066-9227
Data curation (supporting), Investigation (supporting), Visualization (supporting), Writing – review & editing (supporting)

Tadej Rojac 0000-0001-6163-3301
Conceptualization (supporting), Funding acquisition (supporting), Methodology (supporting), Resources (supporting), Supervision (supporting), Validation (supporting), Writing – review & editing (supporting)

Barbara Malič 0000-0002-3438-8846
Methodology (supporting), Resources (supporting), Supervision (supporting), Validation (supporting), Writing – review & editing (supporting)

Mohammad Amirabbasi 0000-0003-1457-8949
Investigation (supporting), Validation (equal), Visualization (supporting), Writing – original draft (supporting), Writing – review & editing (supporting)

Anton Volodin 0009-0004-5528-6023
Formal analysis (supporting), Investigation (supporting), Validation (supporting), Visualization (supporting), Writing – review & editing (supporting)

Karsten Albe 0000-0003-4669-8056
Funding acquisition (supporting), Methodology (supporting), Project administration (supporting), Resources (supporting), Supervision (supporting), Validation (supporting), Writing – review & editing (supporting)

Jurij Koruza 0000-0002-0258-6709
Funding acquisition (supporting), Methodology (supporting), Project administration (supporting), Resources (supporting), Supervision (supporting), Validation (supporting), Writing – review & editing (supporting)

Andreas Klein 0000-0001-7463-1495
Conceptualization (lead), Funding acquisition (lead), Methodology (equal), Project administration (lead), Resources (equal), Supervision (equal), Validation (lead), Visualization (supporting), Writing – original draft (supporting), Writing – review & editing (lead)

References

[1] Sze S M and Ng K K 2007 *Physics of Semiconductor Devices* (Wiley)
[2] Yu P Y and Cardona M 2001 *Fundamentals of Semiconductors* (*Physics and Materials Properties*) 3rd edn (Springer)

[3] Sluka T, Tagantsev A K, Damjanovic D, Gureev M and Setter N 2012 *Nat. Commun.* **3** 748
[4] Zuo Y, Genenko Y A and Xu B-X 2014 *J. Appl. Phys.* **116** 044109
[5] Li L, Salvador P A and Rohrer G S 2014 *Nanoscale* **6** 24–42
[6] Fridkin V M 1980 *Ferroelectric Semiconductors* (Plenum Press)
[7] Klein A *et al* 2023 *J. Electroceram.* **51** 147–77
[8] Bidault O, Maglione M, Actis M, Kchikech M and Salce B 1995 *Phys. Rev. B* **52** 4191
[9] Robertson J, Warren W L and Tuttle B A 1995 *J. Appl. Phys.* **77** 3975–80
[10] Akkopru-Akgun B, Bayer T J M, Tsuji K, Wang K, Randall C A, Lanagan M T and Trolier-McKinstry S 2021 *J. Appl. Phys.* **129** 174102
[11] Schirmer O F, Imlau M, Merschjann C and Schoke B 2009 *J. Phys.: Condens. Matter* **21** 123201
[12] Schirmer O F 2011 *J. Phys.: Condens. Matter* **23** 334218
[13] Khan M, Nadeem M and Idriss H 2016 *Surf. Sci. Rep.* **71** 1–31
[14] Spanier J E *et al* 2016 *Nat. Photon.* **10** 611
[15] Bai Y, Vats G, Seidel J, Jantunen H and Juuti J 2018 *Adv. Mater.* **30** 1803821
[16] Choi T, Lee S, Choi Y J, Kiryukhin V and Cheong S-W 2009 *Science* **324** 63
[17] Lee D, Baek S H, Kim T H, Yoon J-G, Folkman C M, Eom C B and Noh T W 2011 *Phys. Rev. B* **84** 125305
[18] Kreisel J, Alexe M and Thomas P A 2012 *Nat. Mater.* **11** 260–260
[19] Grinberg I *et al* 2013 *Nature* **503** 509
[20] Ji W, Yao K, Lim Y-F, Liang Y C and Suwardi A 2013 *Appl. Phys. Lett.* **103** 062901
[21] Das S, Ghara S, Mahadevan P, Sundaresan A, Gopalakrishnan J and Sarma D D 2018 *ACS Energy Lett.* **3** 1176–82
[22] Fox M 2010 *Optical Properties of Solids* vol 3 (Oxford University Press)
[23] Kubelka P 1931 *Z. Tech. Phys.* **12** 593–601
[24] Tauc J, Grigorovici R and Vancu A 1966 *Physica Status Solidi b* **15** 627–37
[25] Austin I G and Mott N F 1969 *Adv. Phys.* **18** 41–102
[26] Franchini C, Reticcioli M, Setvin M and Diebold U 2021 *Nat. Rev. Mater.* **6** 560–86
[27] Stoneham A M, Gavartin J, Shluger A L, Kimmel A V, Ramo D M N, Rønnow H M, Aeppli G and Renner C 2007 *J. Phys.: Condens. Matter* **19** 255208
[28] Shluger A L and Stoneham A M 1993 *J. Phys.: Condens. Matter* **5** 3049
[29] Natanzon Y, Azulay A and Amouyal Y 2020 *Israel J. Chem.* **60** 768–86
[30] Würfel P 2004 *Physics of Solar Cells* (Wiley)
[31] Klein A 2023 Application of photoelectron spectroscopy to align the energy levels of photocatalysts *Applications of X-ray Photoelectron Spectroscopy to Catalytic Studies* ed S Zafeiratos (World Scientific) pp 193–230
[32] Lohaus C, Klein A and Jaegermann W 2018 *Nat. Commun.* **9** 4309
[33] Thomas D G 1960 *J. Phys. Chem. Solids* **15** 86
[34] Wilson J A and Yoffe A D 1969 *Adv. Phys.* **18** 193–335
[35] Erhart P, Klein A, Aberg D and Sadigh B 2014 *Phys. Rev. B* **90** 035204
[36] Traiwattanapong W, Janotti A, Umezawa N, Limpijumnong S, Thienprasert J and Reunchan P 2018 *J. Appl. Phys.* **124** 085703
[37] Schmidt W G, Albrecht M, Wippermann S, Blankenburg S, Rauls E, Fuchs F, Rödl C, Furthmüller J and Hermann A 2008 *Phys. Rev. B* **77** 035106
[38] Ghorbani E, Villa L, Erhart P, Klein A and Albe K 2022 *Phys. Rev. Mater.* **6** 074410
[39] Schmidt F, Riefer A, Schmidt W G, Schindlmayr A, Imlau M, Dobener F, Mengel N, Chatterjee S and Sanna S 2019 *Phys. Rev. Mater.* **3** 054401
[40] Bein N *et al* 2022 *Phys. Rev. Mater.* **6** 084404
[41] Heeger A J, Kivelson S, Schrieffer J R and Su W P 1988 *Rev. Mod. Phys.* **60** 781–850
[42] Brütting W and Adachi C (eds) 2012 *Physics of Organic Semiconductors* 2nd edn, (Wiley)
[43] Knupfer M 2003 *Appl. Phys. A* **77** 623–6
[44] Bein N S, Machado P, Coll M, Chen F, Makarovic M, Rojac T and Klein A 2019 *J. Phys. Chem. Lett.* **10** 7071–6
[45] Huang B, Erhart P, Yang T and Klein A 2023 *Adv. Mater. Interfaces* **10** 2300332
[46] Hu P, Huang B, Bremecker D, Koruza J, Albe K and Klein A 2024 *J. Appl. Phys.* **136** 114101
[47] Chaoudhary S, Aumen A, Dickey E C and Klein A 2025 *Phys. Rev. Mater.* **9** 075002
[48] Liu Y, Frick S, Lohaus K N S and Klein A 2025 *Phys. Rev. Mater.* **9** 075405
[49] Li M, Pietrowski M J, De Souza R A, Zhang H, Reaney I M, Cook S N, Kilner J A and Sinclair D C 2014 *Nat. Mater.* **13** 31–35
[50] Yang F, Li M, Li L, Wu P, Pradal-Velázquez E and Sinclair D C 2018 *J. Mater. Chem. A* **6** 5243–54
[51] Li L, Li M, Zhang H, Reaney I M and Sinclair D C 2016 *J. Mater. Chem. C* **4** 5779–86
[52] Koch L, Steiner S, Meyer K-C, Seo I-T, Albe K and Frömling T 2017 *J. Mater. Chem. C* **5** 8958–65
[53] Steiner S, Seo I-T, Ren P, Li M, Keeble D J and Frömling T 2019 *J. Am. Ceram. Soc.* **102** 5295–304
[54] Baiatu T, Waser R and Härdtl K-H 1990 *J. Am. Ceram. Soc.* **73** 1663–73
[55] Hu P, Parhi C C, Koruza J and Klein A 2026 Towards understanding the defect properties in the multivalent *A*-site $Na_{0.5}Bi_{0.5}TiO_3$-based perovskite ceramics (arXiv:2601.04725)
[56] Bein N 2024 Electronic structure of sodium niobate - Fermi energy, band gap, defects, and transport properties *PhD Thesis* Technische Universität Darmstadt (https://doi.org/10.26083/tuprints-00027352)
[57] Riemer L *et al* 2017 *Acta Mater.* **136** 271–80
[58] Slabki M, Venkataraman L K, Rojac T, Rödel J and Koruza J 2021 *J. Appl. Phys.* **130** 014101
[59] Seo I-T, Steiner S and Frömling T 2017 *J. Eur. Ceram. Soc.* **37** 1429–36
[60] Aso S, Matsuo H and Noguchi Y 2023 *Sci. Rep.* **13** 6771
[61] Gao L, Guo H, Zhang S and Randall C A 2016 *J. Appl. Phys.* **120** 204102
[62] Zhang M-H *et al* 2023 *Nat. Commun.* **14** 1525
[63] Kresse G and Hafner J 1993 *Phys. Rev. B* **47** 558
[64] Kresse G and Hafner J 1994 *Phys. Rev. B* **49** 14251
[65] Kresse G and Furthmüller J 1996 *Comput. Mater. Sci.* **6** 15–50
[66] Kresse G and Furthmüller J 1996 *Phys. Rev. B* **54** 11169
[67] Blöchl P E 1994 *Phys. Rev. B* **50** 17953
[68] Kresse G and Joubert D 1999 *Phys. Rev. B* **59** 1758

[69] Hedin L 1965 *Phys. Rev.* **139** A796

[70] Perdew J P, Ruzsinszky A, Csonka G I, Vydrov O A, Scuseria G E, Constantin L A, Zhou X and Burke K 2008 *Phys. Rev. Lett.* **100** 136406

[71] Shishkin M and Kresse G 2006 *Phys. Rev. B* **74** 035101

[72] Shishkin M and Kresse G 2007 *Phys. Rev. B* **75** 235102

[73] Shishkin M, Marsman M and Kresse G 2007 *Phys. Rev. Lett.* **99** 246403

[74] Fuchs F, Furthmüller J, Bechstedt F, Shishkin M and Kresse G 2007 *Phys. Rev. B* **76** 115109

[75] Ganose A M *et al* 2025 *Digit. Discovery* **4** 1944–73

[76] Mishchuk D O, V'yunov O I, Ovchar O V and Belous A G 2004 *Inorg. Mater.* **40** 1324–30

[77] Wu G and Neumeier J J 2003 *Phys. Rev. B* **67** 125116

[78] Elliott R J 1957 *Phys. Rev.* **108** 1384

[79] Jubu P R, Yam F K, Igba V M and Beh K P 2020 *J. Solid State Chem.* **290** 121576

[80] Pankove J I 2012 *Optical Processes in Semiconductors* (Courier Corporation)

[81] Kubelka P and Munk F 1931 *Z. Tech. Phys.* **12** 259–74

[82] Landi J S, Segundo I R, Freitas E, Vasilevskiy M, Carneiro J and Tavares C J 2022 *Solid State Commun.* **341** 114573

[83] Jubu P R, Obaseki O S, Ajayi D I, Danladi E, Chahrour K M, Muhammad A, Landi J S, Igbawua T, Chahul H and Yam F 2024 *J. Opt.* **53** 5054–64

[84] Khorrami G H, Kompany A and Zak A K 2015 *Adv. Powder Technol.* **26** 113–8

[85] Kato H, Kobayashi H and Kudo A 2002 *J. Phys. Chem. B* **106** 12441–7

[86] Zhu H *et al* 2006 *J. Am. Chem. Soc.* **128** 2373–84

[87] Li G, Yang N, Wang W and Zhang W 2010 *Electrochim. Acta* **55** 7235–9

[88] Schirmer O F and Von der Linde D 1978 *Appl. Phys. Lett.* **33** 35–35

[89] Sweeney K L and Halliburton L E 1983 *Appl. Phys. Lett.* **43** 336–8

[90] Conradi D, Merschjann C, Schoke B, Imlau M, Corradi G and Polgár K 2008 *Phys. Stat. Sol.* **2** 284–6

[91] Choi G M, Tuller H L and Goldschmidt D 1986 *Phys. Rev. B* **34** 6972

[92] Gröting M, Hayn S and Albe K 2011 *J. Solid State Chem.* **184** 2041–6

[93] Li S *et al* 2013 *Phys. Rev. B* **88** 045428

[94] Huang B, Hu P, Larsson M A, Steinmann J, Yang T, Rojac T and Klein A 2026 *Adv. Mater. Interfaces* **13** e00671

[95] Sun Y, Thompson S E and Nishida T 2010 *Strain Effect in Semiconductors* (Springer)

[96] Li S, Zheng Y, Jakoby R and Klein A 2012 *Adv. Funct. Mater.* **22** 4827–32

[97] Yoo H-I, Song C-R and Lee D-K 2002 *J. Electroceram.* **8** 5–36

[98] Schafranek R, Li S, Chen F, Wu W and Klein A 2011 *Phys. Rev. B* **84** 045317

[99] Rojac T *et al* 2017 *Nat. Mater.* **16** 322

[100] Catalan G and Scott J F 2009 *Adv. Mater.* **21** 2463–85

[101] Hu P *et al* 2026 Data for publication: How semiconducting are ferroelectrics *TU-datalib* (available at: https://tudatalib.ulb.tu-darmstadt.de/handle/tudatalib/5034)